Inorganic Chemistry

Article

pubs.acs.org/IC

The Effect of A-Site Substitution of Ce and La on the Magnetic and Electronic Properties of $Sr(Ti_{0.6}Fe_{0.4})O_{3-\delta}$ Films

Peng Jiang,*[,†,‡] Lei Bi,[‡] Xueyin Sun,[†] Dong Hun Kim,[‡] Daming Jiang,[†] Gaohui Wu,[†] G. F. Dionne,[‡] and C. A. Ross*[,‡]

[†]Department of Materials Science and Engineering, Harbin Institute of Technology, Harbin, 150001, People's Republic of China

[‡]Department of Materials Science and Engineering, Massachusetts Institute of Technology, Cambridge, Massachusetts 02139, United States

ABSTRACT: The structure and magnetic properties of epitaxial $(Ce_xSr_{1-x})(Ti_{0.6}Fe_{0.4})O_{3-\delta}$ (x = 0, 0.1, 0.2 and 0.3) and $(La_xSr_{1-x})(Ti_{0.6}Fe_{0.4})O_{3-\delta}$ (x = 0, 0.1, 0.2, 0.3 and 0.4) perovskite-structure thin films deposited by pulsed laser deposition on $(LaAlO_3)_{0.3}(Sr_2AlTaO_6)_{0.7}$ (LSAT) substrates are reported. Both La and Ce ions showed a dominant 3+ valence state and acted as donors on the Sr^{2+} site (A site) in the perovskite lattice. The optical band gap widened, and the Fermi level moved toward the vacuum level with increased Ce or La content; meanwhile the Ti and particularly the Fe ions were driven to a lower valence state, resulting in a higher Fe^{2+} concentration. The materials were magnetic at room temperature with up to 0.8 μ_B/Fe and a magnetoelastic out-of-plane anisotropy. Ce and La lowered the coercivity while raising both the Faraday rotation at 1550 nm and the optical absorption at near-infrared wavelengths.

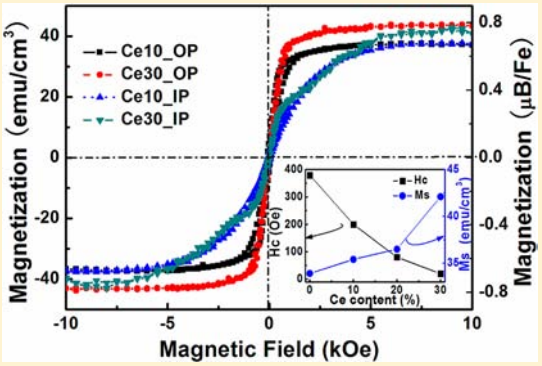

I. INTRODUCTION

Room temperature ferrimagnetic oxides such as iron garnets, spinels and hexaferrites are widely used in nonreciprocal optical and microwave devices. Despite their success in commercial bulk devices, these materials do not have a good lattice and thermal match with semiconductor substrates, such as Si or GaAs,[1,2] and it can be difficult to integrate them directly on a semiconductor platform. Perovskite-structured oxides can be epitaxially deposited on silicon coated with oxide buffer layers, and magnetic substitution can lead to intrinsic ferromagnetism, high resistivity and significant magneto-optical effects at near-infrared wavelengths, which makes them promising candidates for integrated optical devices. Room temperature ferromagnetism has been reported in various perovskite systems, such as $Ba(Ti_{1-x}Fe_x)O_3$,[3−5] $Ba(Zr_{1-x}Fe_x)O_3$,[6] $Sr(Ti_{1-x}Fe_x)O_3$,[7] $La_{0.35}Sr_{0.65}(Ti_{1-x}Fe_x)O_3$,[8] $Sr(Ti_{1-x}Co_x)O_3$[9] and $Ba(Sn_{1-x}Fe_x)O_3$.[10]

Among these materials, $Sr(Ti_{1-x}Fe_x)O_3$ (STF) films show high Faraday rotation as well as moderate optical absorption at near-infrared wavelengths.[7] A figure of merit (Faraday rotation divided by optical absorption) of 1.1 deg/dB was measured for a $Sr(Ti_{0.6}Fe_{0.4})O_3$ film at 1550 nm, exceeding that of Fe_3O_4 but smaller than that of garnets. In order to improve the figure of merit further, one needs to either increase the Faraday rotation or decrease the optical absorption. We showed earlier that B-site substitution of Ga^{3+} for Ti^{4+} in STF raised the average valence state of Fe and improved the figure of merit by lowering optical absorption, though it also lowered the magnetization.[11] It is well-known that Bi^{3+} or Ce^{3+} doping in the dodecahedral site of $Y_3Fe_5O_{12}$ (YIG, yttrium iron garnet) significantly increases the material's figure of merit, so it is interesting to examine the effects of these and other substituents on the optical and magnetic properties of STF. In this article, we describe the magnetic and magneto-optical properties and the electronic structure of $(Ce_xSr_{1-x})(Ti_{0.6}Fe_{0.4})O_{3-\delta}$ (CeSTF) and $(La_xSr_{1-x})(Ti_{0.6}Fe_{0.4})O_{3-\delta}$ (LaSTF) films as a function of Ce and La concentration. With increasing Ce and La concentration, the material showed higher saturation magnetization, Faraday rotation and optical absorption and lower coercivity, and these effects are discussed in terms of changes in the Fe valence states.

II. EXPERIMENTAL METHODS

$(Ce_xSr_{1-x})Ti_{0.6}Fe_{0.4}O_3$ (x = 0, 0.1, 0.2 and 0.3, identified as STF40, Ce10, Ce20 and Ce30) and $(La_xSr_{1-x})(Ti_{0.6}Fe_{0.4})O_3$ (x = 0, 0.1, 0.2, 0.3, and 0.4 identified as STF40, La10, La20, La30 and La40) targets were prepared by pressing La_2O_3, TiO_2, Fe_2O_3, CeO_2 and $SrCO_3$ powders after calcination at 1350 °C for 3 h. Pulsed laser deposition (PLD) was carried out using a Coherent COMPexPro 205 KrF (248 nm) excimer laser at 10 Hz and 2 J/cm² fluence on $(LaAlO_3)_{0.3}(Sr_2AlTaO_6)_{0.7}$ (LSAT) (001) substrates held at 750 °C. LSAT substrates were selected to provide a good quality single crystal substrate on which epitaxial growth could occur, while being sufficiently transparent to allow optical transmittance and Faraday rotation measurements to be performed. Our prior work has shown generally similar properties of STF grown on Si buffered with yttria-

Received: August 7, 2012
Published: December 4, 2012

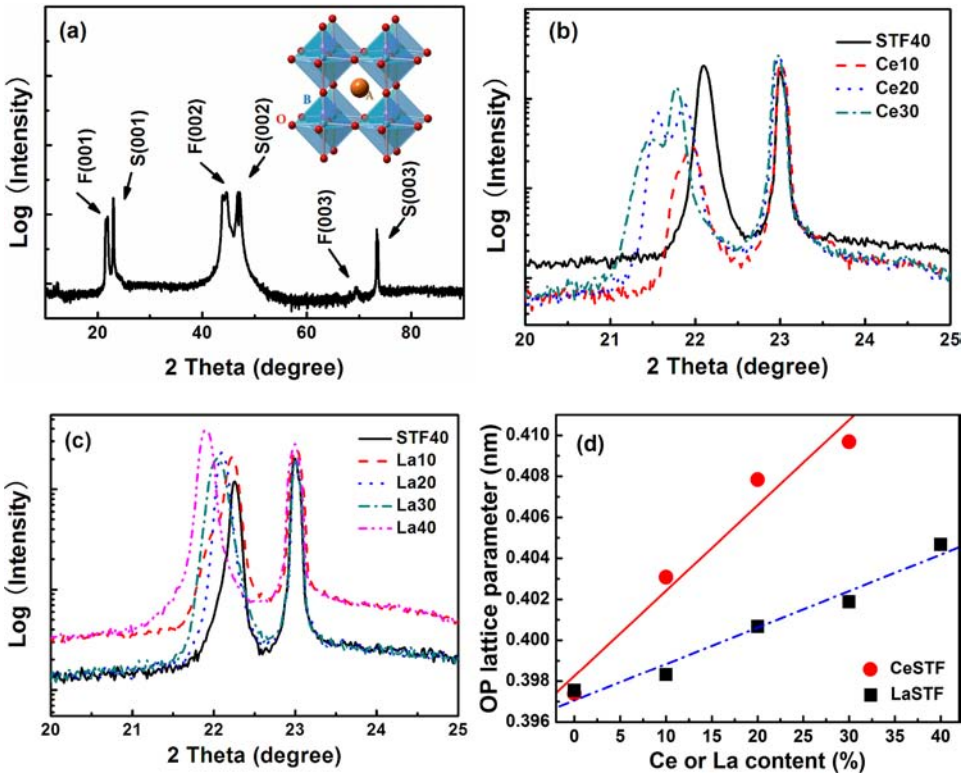

Figure 1. X-ray diffraction patterns of $Sr(Ti_{0.6}Fe_{0.4})O_{3-\delta}$, $(Ce_xSr_{1-x})(Ti_{0.6}Fe_{0.4})O_{3-\delta}$ and $(La_xSr_{1-x})(Ti_{0.6}Fe_{0.4})O_{3-\delta}$ films. (a) $\omega-2\theta$ X-ray diffraction patterns of STF40; the inset shows typical ABO_3 pervoskite structure. F(00l) and S(00l) indicate the (00l) diffraction peaks from the film and substrate respectively. (b) (001) diffraction peak of the CeSTF films. (c) (001) peak of the LaSTF films. (d) The out-of-plane lattice parameter of CeSTF and LaSTF films.

stabilized zirconia/ceria compared to films on STO.[12−14] The deposition took place in vacuum with a pressure of 2.0×10^{-6} Torr at a rate of 5−6 nm/min. After deposition, the substrate was cooled down to room temperature in vacuum at a rate of 5 °C/min.

The thickness of the films was ∼250 nm measured on a profilometer. Phase identification and texture analysis was carried out using X-ray diffraction. Conventional $\omega-2\theta$ Bragg diffraction scans were collected on a Rigaku RU300 diffractometer. X-ray reciprocal space mapping (RSM) was done on a Bruker HRXRD system with Ge(022)×4 monochromator. X-ray photoelectron spectroscopy (XPS) was performed on a Kratos Axis Ultra spectrometer with a monochromated Al Kα source and a hemispherical analyzer. The high resolution spectrum at the Co K-edge was measured with a pass energy of 20 eV and an energy resolution of 0.3 eV.

Room temperature magnetic hysteresis loops were characterized by vibrating sample magnetometry (VSM) using an ADE Technologies VSM model 1660. The low temperature magnetic properties were measured using a superconducting quantum interference device magnetometer (SQUID, Quantum Design), at temperatures of 5 to 300 K and in fields up to 50 kOe. Faraday rotation hysteresis loops were measured at 1550 nm on a custom-built apparatus at room temperature, with the field and light propagation directions perpendicular to the film.[4] Optical transmission spectra were recorded on a Cary 500i UV−vis−NIR dual-beam spectrophotometer at 200−2000 nm wavelength. The electrical transport properties were characterized by surface resistivity measurements using the Van der Pauw method at room temperature.

Stoichiometry was measured by wavelength dispersive spectroscopy (WDS). The films were deficient in Ce, La and Fe compared to the targets, and had measured compositions of $Sr(Ti_{0.67}Fe_{0.33})O_{3-\delta}$ for the sample from target STF40, $(Ce_{0.06}Sr_{0.94})(Ti_{0.67}Fe_{0.33})O_{3-\delta}$ for Ce10, $(Ce_{0.17}Sr_{0.83})(Ti_{0.66}Fe_{0.34})O_{3-\delta}$ for Ce20, $(Ce_{0.28}Sr_{0.72})(Ti_{0.66}Fe_{0.34})$-$O_{3-\delta}$ for Ce30, $(La_{0.06}Sr_{0.95})(Ti_{0.67}Fe_{0.33})O_{3-\delta}$ for La10, $(La_{0.15}Sr_{0.85})$-$(Ti_{0.66}Fe_{0.34})O_{3-\delta}$ for La20, $(La_{0.25}Sr_{0.75})(Ti_{0.66}Fe_{0.34})O_{3-\delta}$ for La30 and $(La_{0.35}Sr_{0.65})(Ti_{0.66}Fe_{0.34})O_{3-\delta}$ for La40. δ represents the oxygen deficiency in vacuum-deposited films. Samples for transmission electron microscopy (TEM) were prepared using a focused ion beam (FEI-600) and then observed on a FEI G^2 F30 transmission electron microscope at 300 kV. The composition of the Ce30 sample was analyzed by high angle annular dark-field scanning transmission electron microscope (HAADF-STEM).

III. RESULTS AND DISCUSSION

A. Crystal Structure of Films. One dimensional X-ray diffraction data from the films are shown in Figure 1a for STF40, Figure 1b for the CeSTF series and Figure 1c for the LaSTF series. F(00l) and S(00l) indicate the diffraction peaks from the (00l) planes of the film and substrate respectively. All the films crystallized into a perovskite phase, and no secondary phase diffraction peaks were observed. This is consistent with previous reports that A-site doping elements Ce and La are fully soluble in the perovskite structure.[15,16] Compared with the ionic radii[17] of B-site ions Ti^{3+}(VI) (0.67 Å), Ti^{4+}(VI) (0.605 Å), Fe^{2+} (hs,VI) (0.770 Å) and Fe^{3+} (hs,VI) (0.645 Å), Ce^{4+} (VIII) (0.97 Å), Ce^{3+} (XII) (1.29 Å) and La^{3+} (XII) (1.32 Å) ions are larger and are more likely to substitute for Sr^{2+} (XII) (1.44 Å) ions in the A sites. A "cube-on-cube" orientation relationship is expected between the film and the substrate. In Figure 1b and Figure 1c, which show the magnified (001) diffraction peaks for Ce- and La-substituted STF40, respectively, the (001) peaks consistently shifted to lower 2θ angles with increasing Ce or La concentration, indicating an expansion in the out of plane lattice constants. The film (00l) diffraction peaks for the CeSTF series split into two peaks, but those of the LaSTF did not. The out-of-plane (c-axis) lattice parameters are shown in Figure 1d.

dx.doi.org/10.1021/ic301726w | Inorg. Chem. 2012, 51, 13245−13253

To understand the film strain and XRD peak splitting quantitatively, an X-ray reciprocal space map (RSM) was measured on the (103) peaks of the Ce20 film, Figure 2. Both

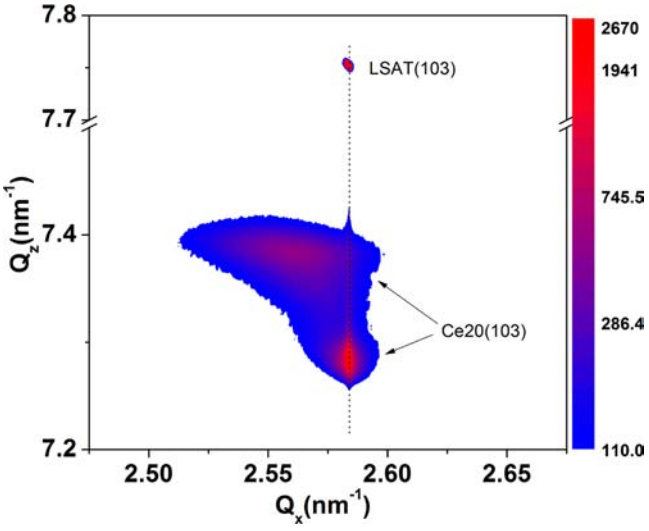

Figure 2. X-ray reciprocal space map of the (103) diffraction peak of the Ce20 film and the LSAT substrate. The color scale is a log scale of peak intensity (in arbitrary units). Q represents the scattering vector.

the substrate and the film show spotlike diffraction patterns, suggesting that the film was epitaxial on the substrate. The film diffraction pattern consisted of two spots, one of which showed the same in-plane lattice constant compared with the substrate, and the other showed a broader diffraction spot with a larger in-plane lattice constant. This suggests that the film consisted of two layers with different strain states. We propose that, during deposition, initially the film grew coherently on the substrate with a compressively strained state. When the film thickness exceeded a critical value, the strain was partially relaxed by a mechanism such as dislocation or defect generation, compositional inhomogeneity, twinning or some other process. The broadening of the diffraction spot corresponds to a higher defectivity in the relaxed regions. To confirm this hypothesis, 50 vol % H_3PO_4 was used to remove the surface layers of the film. With increasing etch time, one of the double diffraction peaks in the $\omega-2\theta$ X-ray patterns diminished. After 7 min etch, only the diffraction peak with larger out-of-plane lattice parameter was present, confirming that the more highly strained layer was deposited first and the more relaxed layer formed after the film had reached a certain thickness.

The in-plane and out-of-plane lattice parameters of the Ce20 film and substrate were calculated from the RSM peak positions. The substrate was cubic with a lattice parameter of 3.87 ± 0.004 Å. The highly strained film layer had an in-plane lattice parameter of 3.87 ± 0.004 Å and out-of-plane lattice parameter of 4.08 ± 0.004 Å, i.e., c/a = 1.054 ± 0.002; while the partly relaxed layer had an in-plane lattice parameter of 3.91 ± 0.004 Å and out-of-plane lattice parameter of 4.05 ± 0.004 Å, i.e., c/a = 1.036 ± 0.002. The unit cell volumes were V = 61.11 ± 0.02 Å^3 (highly strained layer) and 61.91 ± 0.02 Å^3 (partly relaxed layer), i.e., the pseudocubic lattice parameters $V^{1/3}$ were 3.938 Å and 3.956 Å. The highly strained layer was coherent with the substrate, i.e., strained in-plane by about 2%.

B. Transmission Electron Microscopy and Compositional Homogeneity. The TEM and HADDF-STEM images of the Ce30 film and the LSAT substrate are shown in Figure 3. The thickness is about 150 nm, and the interface between the LSAT substrate and the Ce30 film is clear. The Ce30 film shows columnar growth, Figure 3a. Comparing the diffraction patterns, the orientation of the crystal structure in the film is

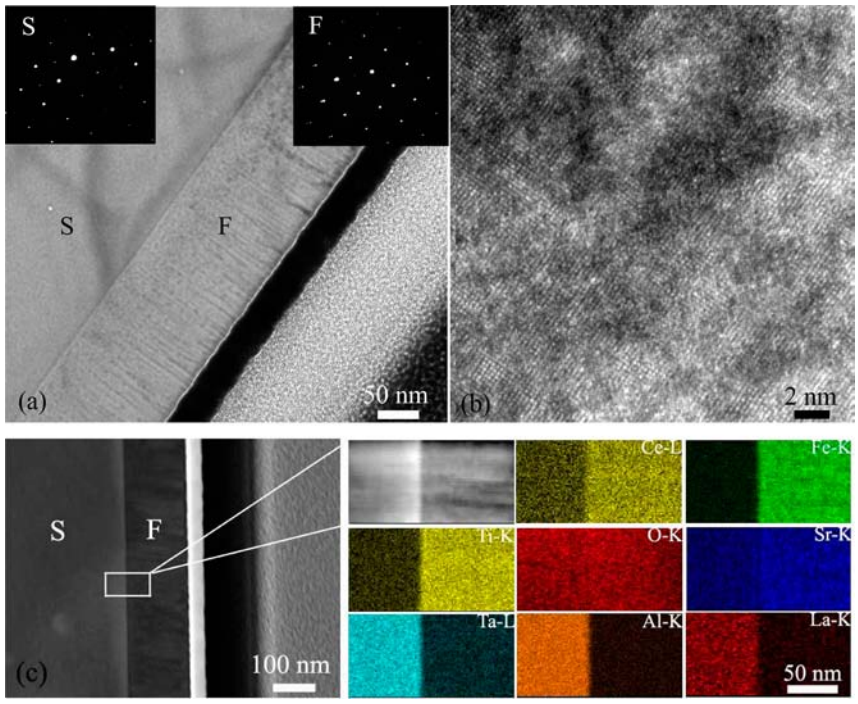

Figure 3. Transmission electron microscopy (TEM) and high angle annular dark-field scanning transmission electron microscope (HAADF-STEM) images of the Ce30 film and the LSAT substrate. (a) Bright field TEM image and diffraction patterns (S, substrate; F, film); (b) HRTEM image of the film; (c) HAADF-STEM images of the Ce30 film and the LSAT substrate showing signals from several elements.

dx.doi.org/10.1021/ic301726w | Inorg. Chem. 2012, 51, 13245−13253

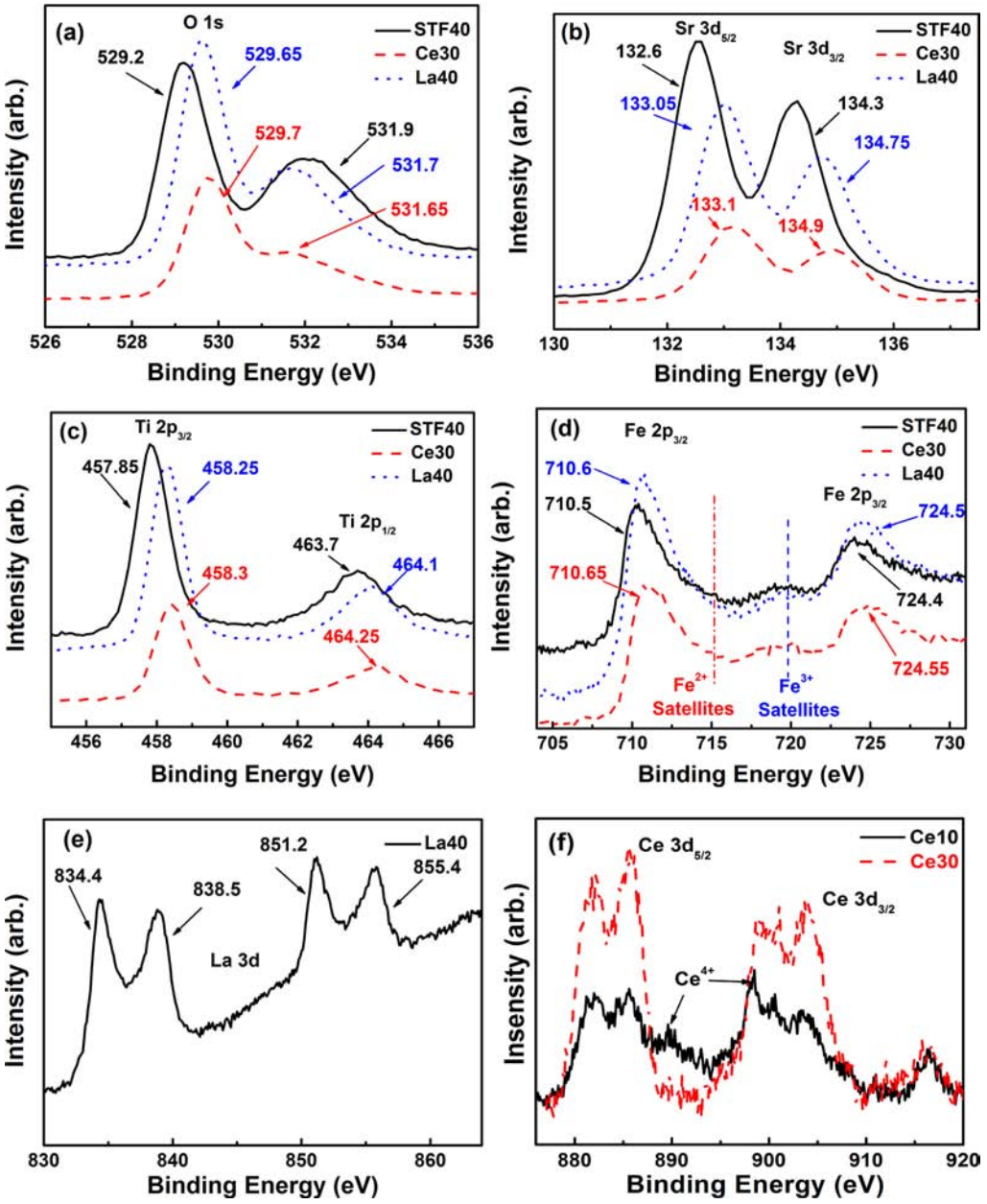

Figure 4. XPS spectra of STF40, Ce30 and La40 samples showing the core level spectra of (a) O 1s, (b) Sr 3d, (c) Ti 2p and (d) Fe 2p; (e) the core level spectra of La 3d for La40; (f) the core level spectra of Ce 3d for Ce10 and Ce30 samples.

the same as that in the substrate, while the lattice parameters are slightly different, which is in accord with the X-ray diffraction patterns of Ce20. A high resolution TEM image of the film is shown in Figure 3b, with no indications of clustering. The HAADF-STEM images of the Ce30 film and the LSAT substrate are shown in Figure 3c. The Ce, Fe and Ti are only present in the film, and their distributions are homogeneous. The Al, La and Ta are only present in the substrate. O appears homogeneous in both the substrate and film. The content of Sr in the film is slightly greater than that in the substrate. The interpretation is that there is no significant interdiffusion between the film and substrate, and that the film has no compositional inhomogeneity detectable by this technique.

C. Conductivity and Electronic Structure. All the films were insulators at room temperature. For STF40, Ce10, Ce20 and all the LaSTF40 samples, the film resistivity was estimated to be higher than 10^{10} Ω/cm^2 for films ~250 nm thick, and they were too insulating to enable sufficient current injection for carrier concentration measurements. For Ce30, the film resistivity was 3.30×10^8 Ω/cm^2, giving a resistivity of 6.39×10^3 Ω cm. Hall measurement indicated that the film was an n-type conductor with a carrier concentration of 2.59×10^{14} cm^{-3} and carrier mobility of 3.79 cm^2 V^{-1} s^{-1}. These results suggest that the Ce acted as a donor in the perovskite lattice.

The electronic structure of selected films was characterized by XPS. Figure 4a–d shows the XPS core level spectra of O 1s, Sr 3d, Ti 2p, Fe 2p in the STF40, Ce30 and La40 samples. The binding energies (BE) were corrected by offsetting the spectra using the surface contamination C 1s peak at 285.0 eV as a reference (not shown). Although the C 1s peak shape and position for all samples was very similar, a clear chemical shift of the BE was observed for the other elements. Compared with STF40, the O 1s, Sr 3d and Ti 2p peaks shifted 0.45 eV, 0.45 eV, 0.40 eV for La40, and 0.50 eV, 0.50 eV, 0.45 eV for Ce30

dx.doi.org/10.1021/ic301726w | Inorg. Chem. 2012, 51, 13245–13253

respectively toward higher BE; whereas the Fe 2p peaks only shifted upward by around 0.10 eV for La40 and 0.15 eV for Ce30. (The weaker O 1s peak observed around 531.5 eV originated from surface-adsorbed OH species and remained at almost the same position.[18])

For the La40 film, the La ions only had 3+ valence state. The La core level 3d peaks were situated at 834.4 eV, 838.5 eV, 851.2 eV and 855.4 eV shown in Figure 4e, which was consistent with another report in which the C-contamination 1s peak was also at 285.0 eV.[19] By comparing the shape and peak positions of the Ce 3d peaks of Figure 4f, the valence state of Ce ions appeared to be different in the Ce10 and Ce30 samples.[20] In Ce10, Ce was in a mixed-valence state of Ce^{4+} and Ce^{3+}. This was deduced from both the Ce^{3+}-like spectrum shape and the two Ce^{4+} 3d peaks at around 890 and 897 eV. However, in Ce30 the two Ce^{4+} 3d peaks weakened or disappeared, and the Ce was mostly in the 3+ valence state.

The Ti 2p core level peaks are at 458.3 ± 0.1 eV for Ti^{4+} and 456.3 ± 0.1 eV for Ti^{3+}.[15] From Figure 4c, the Ti in the La40 and Ce30 samples was almost completely Ti^{4+}, but in the STF40 sample it was present as mixed-valence Ti^{3+} and Ti^{4+}.

Figure 4d shows the Fe 2p line. The peak position is expected to be around 719.2 eV for Fe^{3+} and 715.2 eV for Fe^{2+}.[21,22] The peak binding energy of the first 2p peak measured for Fe_2O_3 is at 710.8 ± 0.1 eV.[23,24] The XPS measurements revealed that the Fe in the three samples was present as mixed-valence Fe^{2+} and Fe^{3+}. The presence of Fe with valence below 4+ in the STF40 occurs as a result of the oxygen deficiency, since Fe adopts lower valence states more readily than does Ti. Substituting Ce or La on the A sites drives a further reduction in the Fe valence because the Ce and La ions have a higher valence state than the Sr^{2+} which they replace. For samples with La or Ce, the first 2p peaks are at 710.5−710.65 eV, which is slightly lower than for Fe_2O_3 powders, suggesting Fe^{3+} was the dominant valence in all samples.

These variations of the XPS spectra and electronic transport properties provide insight into the evolution of the electronic structure caused by Ce or La substitution. Since Ce is mostly in the 3+ valence state in the Ce30 sample, the n-type conductivity is consistent with Ce substituting on the Sr^{2+} A site. In the XPS data, the chemical shift of the binding energy ΔE of a core level can be expressed as $\Delta E = \Delta\mu + K\Delta Q + \Delta V_M + \Delta E_R$,[25,26] where $\Delta\mu$ is the Fermi energy shift, ΔQ is the valence electron variation on the atom considered, K is the Coulomb interaction coupling constant between the valence and the core electrons and ΔV_M is the change in the potential energy of the photoionized atom in the crystal lattice, which can be simplified to a Madelung type energy in these insulating films. ΔE_R is the change of relaxation energy of the other electrons caused by creating a photoelectron in the atom, which is due to changes in the screening effect from metallic conduction electrons and polarizable surrounding ions of the core hole potential.[19] The binding energy shift of the ions in the samples can originate from one or more of these terms. Considering that Sr and O remain in 2+ and 2− valence states respectively, there is little contribution of ΔQ to ΔE from these two ions. Also ΔE_R is negligible since the films were highly insulating with a maximum carrier concentration in the Ce30 sample of $\sim 10^{14}$ cm^{-3} electrons/cm^{-3}.[27] The chemical shift of Sr 3d and O 1s peaks was similar for La30 and Ce30 (0.45 eV for La30 and 0.50 eV for Ce30), which ruled out an observable contribution from the ΔV_M term. This is because, by introducing Ce or La in the lattice, the average charge of the Sr/Ce or Sr/La sites and O sites would be $(2 + x)$+ and 2− respectively if all the Ce or La were in the 3+ valence state. Due to different dependences of the Madelung energy of the Sr/Ce or Sr/La site and O site on the Ce or La concentration x, if ΔV_M had a significant contribution to ΔE, the chemical shift of Sr 3d and O 1s peaks should have been different, which was not observed. The quenching of ΔV_M is possibly due to redistribution of electric charges.[27] Therefore from the above analysis, we can conclude that the Fermi energy shift was the main reason for the chemical shift of the Sr 3d and O 1s peaks. By increasing the Ce or La concentration, the Fermi level shifted 0.50 eV/0.45 eV toward the vacuum level in Ce30/La40 respectively compared to STF40. Unlike Sr and O, Ti and Fe showed smaller chemical shifts in both La40 and Ce30 samples. Since ΔE_R and ΔV_M are negligible, this difference is attributed to the valence electron variation ΔQ of the two ions, i.e., the valence states. Since $\Delta\mu$ is identical for all ions, the $K\Delta Q$ term in both La40 and Ce30 samples was calculated to be −0.10 eV and −0.35 eV for Ti and Fe respectively. Both values are negative, indicating that both ions were reduced to a lower valence state by Ce or La doping. This is consistent with the donor behavior of Ce from electronic transport measurements.

D. Magnetic Measurements. Room temperature ferromagnetic hysteresis was observed in all samples. Figure 5a shows the out-of-plane and in-plane magnetic hysteresis loops of Ce10 and Ce30 films measured by VSM at room temperature, while the data for STF40 is in Figure 5b. Similar to other STF films fabricated in vacuum,[7] the films here all showed an out-of-plane easy axis, with in-plane saturation fields exceeding 5−6 kOe. The saturation magnetization of the films

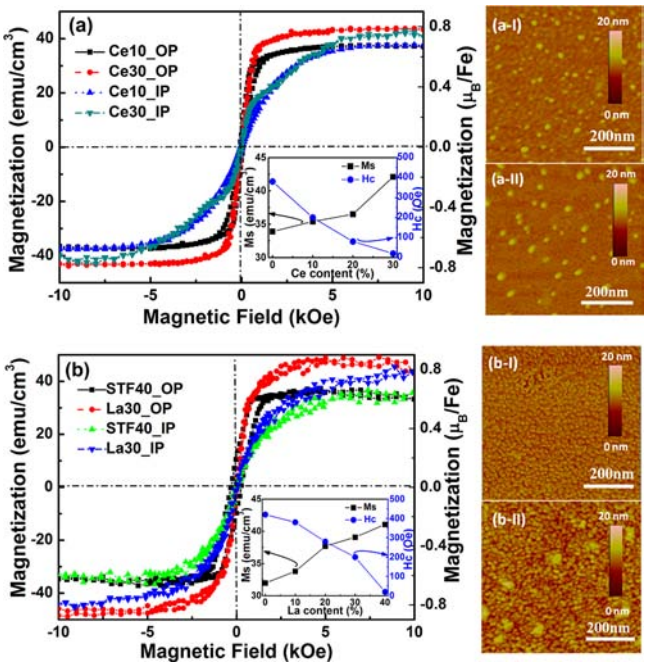

Figure 5. Room temperature out-of-plane and in-plane hysteresis loops of films characterized by VSM. The insets show the coercivity and saturation magnetization of the out-of-plane magnetic hysteresis loops as a function of the Ce or La concentration. (a) Ce10 and Ce30 films and (b) STF40 and La30 films. Atomic force microscopy (AFM) of the Ce or La doped STF40 films. (a-I) Ce10 film, (a-II) Ce30 film, (b-I) STF40 film and (b-II) La30 film.

dx.doi.org/10.1021/ic301726w | Inorg. Chem. 2012, 51, 13245−13253

increased slightly with Ce concentration, with a larger increase in M_s observed in the Ce30 sample, and the out-of-plane coercivity decreased with Ce content.

Figure 5b shows the hysteresis loops for La30 at room temperature. All the LaSTF films showed an out-of-plane magnetic anisotropy, and in-plane saturation occurred well above 5 kOe. Other compositions gave similar loops to those of La30, though the coercivity decreased and saturation moment increased with La content, similar to the case of CeSTF.

The coercivity of STF, CeSTF and LaSTF in this study is lower than that reported previously for STF films.[7,11] Figures 5a-I, 5a-II, 5b-I and 5b-II show atomic force microscopy (AFM) of Ce10, Ce30, STF40 and La30 films, respectively. Despite being epitaxial the films show some surface roughness, on a length scale of 20 to 25 nm. The roughness shows little variation between the samples, which suggests that the systematic decrease in H_c is not an extrinsic effect from changes in domain wall pinning by surface roughness. It may represent changes in the net anisotropy or the exchange strength which affect the domain wall energy.

The out-of-plane easy axis is consistent with magnetoelastic anisotropy caused by the compressive strain state of the films, as discussed elsewhere for STF and similar materials,[7,9,11,12,25] and for epitaxial manganate thin films such as $(La,Sr)MnO_3$[28,29] and $(La,Ca)MnO_3$[30,31] in which magnetoelasticity arises from the Mn^{3+} ions.[12,30,31] In (001) STF films, magnetoelastic Fe^{2+} or Fe^{4+} promotes an out-of-plane easy magnetic axis under an in-plane compressive strain,[12,32−36] which corresponds to a positive magnetostriction coefficient λ_{001}. Orientation-dependent measurements of anisotropy of epitaxial $SrTi_{0.65}Fe_{0.35}O_{3-\delta}$ films on $SrTiO_3$ gave a value for $\lambda_{001} \sim 0.6 \times 10^{-6}$ (corresponding to a magnetoelastic coefficient $B_1 = -6.7 \times 10^6$ erg/cm^3) and showed that magnetocrystalline and shape anisotropies are small compared with magnetoelastic anisotropy.[37] Although the magnetostriction is modest, the large epitaxial mismatch strains lead to high magnetoelastic anisotropy. In the present samples, for the Ce30 the anisotropy field $H_K \sim 5$ kOe. Taking $H_K = 2K/M_s$, where the major contribution to anisotropy K is the magnetoelastic anisotropy $B_1(\varepsilon_{xx} - \varepsilon_{zz})$ with ε_{xx} the in-plane and ε_{zz} the out-of-plane strain taken as those of the unrelaxed layer, yields $B_1 \sim -2 \times 10^7$ erg/cm^3, about three times larger than that of the STF35 of ref 37. The Ce30 in-plane loop shows a distinct slope change, and it is possible this may reflect two different anisotropies from the strained and partly relaxed layers.

The magnetoelastic anisotropy appeared to increase as Ce and La were substituted, although the in-plane saturation fields cannot be determined accurately from the slow approach to saturation of the in-plane loops. An increase in magnetoelastic anisotropy would be expected from the increasing film strain as the lattice parameter expands, but changes in the relative amounts of Fe ions are also important in determining the anisotropy. An increase in Fe^{2+}/Fe^{3+} ratio driven by La and Ce substitution would enhance the magnetoelasticity since Fe^{3+} is not a magnetoelastic ion.[12]

E. Magneto-Optical and Optical Properties. Figure 6 shows the out-of-plane room temperature Faraday rotation (FR) hysteresis loops of the films at 1550 nm wavelength. The magneto-optical hysteresis loops resembled the magnetic loops, although the loop coercivity H_{cF} was larger in all samples, which is similar to our previous report for STF films.[7] The saturation FR, Θ_F, increased for La and for the highest Ce and La concentration, and H_{cF} decreased with La and Ce, following the

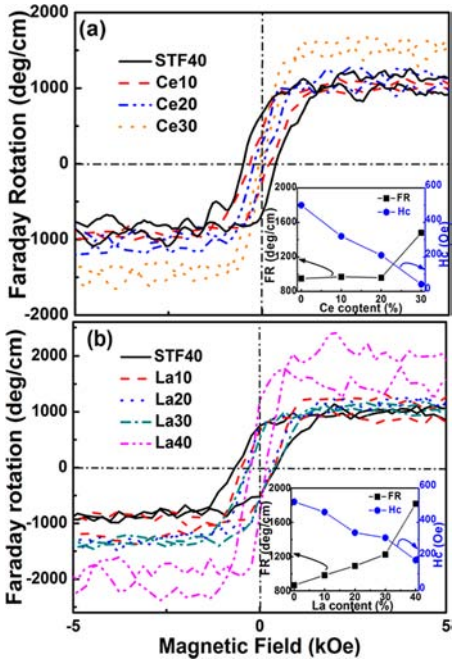

Figure 6. Room temperature Faraday rotation of films. The insets show the coercivity and saturation Faraday rotation at 10 kOe as a function of the Ce or La concentration. (a) CeSTF films and (b) LaSTF films.

trends seen in the MH loops. However, the changes in Θ_F and H_{cF} were more dramatic than those in the MH loops. The Θ_F reached ∼1800 deg/cm for La40, double that of the STF40, and 1500 deg/cm for Ce30, about 1.5 times that of STF40. These results can be compared with magnetic garnets, where Ce contributes dramatically to the FR in the near-IR so that CeYIG has more than 10 times greater FR than YIG.[38,39] In our perovskites, although Ce raises Θ_F, La has a similar effect so the change in Θ_F is not related to the presence of Ce *per se*. The increases in Θ_F may just be caused by the increase in lower-valence Fe. Fe^{2+} in the octahedral site of yttrium iron garnet shows a characteristic transition at near-infrared wavelengths contributing both to FR and to optical absorption,[40,41] and a similar mechanism may be at play in the CeSTF and LaSTF.

The optical transmittance spectra of CeSTF and LaSTF films are shown in Figure 7a,b, where the inset provides detail near the optical band gap. Increasing Ce and La concentration increased the band gap. The optical band gap of STF40, Ce10, Ce20 and Ce30 films was estimated to be 3.69 eV, 3.73 eV, 3.83 and 3.90 eV, and 3.73, 3.76, 3.84, and 3.90 eV for La10, La20, La30 and La40 films respectively (shown in insets of Figure 7c,d). The transmission spectra showed interference oscillations due to film thickness, but there was also a consistent drop in transmittance around 600 nm wavelength for films containing Ce and La. This absorption peak has been observed in Ce^{3+}-doped $SrTiO_3$ and was attributed to an interatomic electronic transition between Ce^{3+} and Ti^{4+} ions.[42] Finally, in the near-infrared, the optical transmittance decreased with increasing Ce and La concentration. This is not due to free carrier absorption considering that the samples are highly insulating, and instead is attributed to the reduction of the average valence state of Fe ions and the consequent optical absorption from Fe^{2+} ions. This result may be compared with Ga-substituted STF, where Ga^{3+} substituted for Ti^{4+} *raised* the average Fe valence state and *lowered* optical absorption.[11]

dx.doi.org/10.1021/ic301726w | *Inorg. Chem.* 2012, 51, 13245−13253

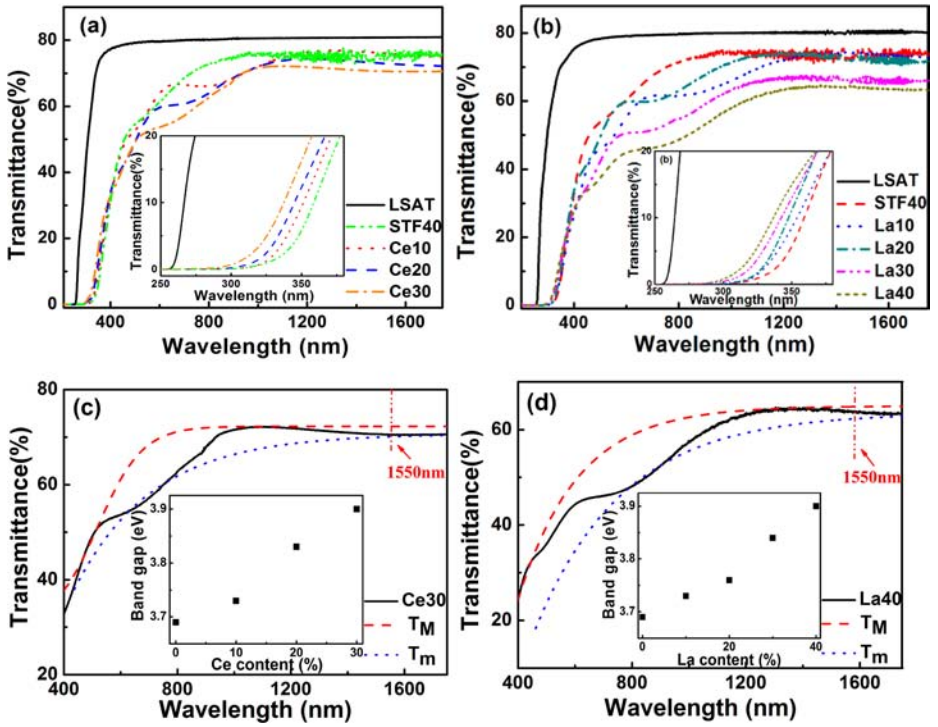

Figure 7. Optical transmittance spectrum of films measured by UV−vis−NIR spectrophotometer at room temperature. (a) $(Ce_xSr_{1-x})(Ti_{0.6}Fe_{0.4})O_{3-\delta}$ films and (b) $(La_xSr_{1-x})(Ti_{0.6}Fe_{0.4})O_{3-\delta}$ films. The insets show the magnified spectrum near the optical band gap; the extreme of interference fringes T_M and T_m fitted by nonliner curves. (c) $(Ce_xSr_{1-x})(Ti_{0.6}Fe_{0.4})O_{3-\delta}$ films and (d) $(La_xSr_{1-x})(Ti_{0.6}Fe_{0.4})O_{3-\delta}$ films. The insets show the optical band gap as a function of the Ce or La concentration.

The transmittance loss at 1550 nm wavelength is hard to obtain from UV−vis curves due to the optical interference. It is necessary to know the refractive index n and absorption coefficient α of the films. The films' refractive index n was calculated by eq 1,[43]

$$n = [N + (N^2 - s^2)^{1/2}]^{1/2} \quad (1)$$

where s is the substrate refractive index and N is found from eq 2,

$$N = 2s\frac{T_M - T_m}{T_M T_m} + \frac{s^2 + 1}{2} \quad (2)$$

where T_M is the maximum transmittance of the interference fringes and T_m is the minimum of the interference fringes which could be fitted as in ref 43.

The absorbance x of the films is given by eq 3,[43]

$$x = \frac{E_M - [E_M{}^2 - (n^2 - 1)^3(n^2 - s^4)]^{1/2}}{(n - 1)^3(n - s^2)} \quad (3)$$

where

$$E_M = \frac{8n^2 s}{T_M} + (n^2 - 1)(n^2 - s^2) \quad (4)$$

The absorption coefficient α of the films was calculated by eq 5,[43]

$$x = \exp(-\alpha d) \quad (5)$$

where d is the film thickness.

For La40 and Ce30 films, the extreme of interference fringes T_M and T_m fitted by nonlinear curves as ref 43 is shown in Figure 7c,d. The maximum T_M and minimum T_m of the interference fringes at 1550 nm wavelength were 0.725 and 0.707 for Ce30 and 0.648 and 0.622 for La40 respectively. The substrate LSAT refractive index s is ~2.0.[44] Therefore, the films' refractive index n and absorbance x at 1550 nm wavelength were 2.089 and 0.909 for Ce30 and 2.158 and 0.818 for La40 respectively. Meanwhile, the absorption coefficient α was 3790 cm^{-1} for Ce30 and 8036 cm^{-1} for La40 respectively. To relate α to absorption loss α_{dB} [dB/cm] eq 6 applies:

$$\begin{aligned} -\alpha_{dB} \cdot d &= 10 \log_{10} x \\ &= 10 \log_{10}(e^{-\alpha d}) \\ &= -10\alpha d \log_{10} e \\ &= -4.34 d\alpha \end{aligned} \quad (6)$$

So $\alpha_{dB} = 4.34\alpha$ was obtained.[45] The figure of merit for the film was then estimated as FOM = $\Theta_F/4.34\alpha$, and the values could be obtained as 0.092 deg/dB for Ce30 and 0.052 deg/dB for La40. Though Θ_F increased with La or Ce, the rapidly increasing transmittance loss caused the FOM to fall with increasing La or Ce content.

F. Low Temperature Magnetic Properties. Low temperature magnetic properties were characterized for the LaSTF films. Analysis of the CeSTF is complicated by the $4f^1$ magnetism from the Ce^{3+} ions. Figure 8a shows in-plane magnetic hysteresis loops measured at 5 K for La30 and STF40. The La30 had a higher moment, and required a higher field, of order 20 kOe, to saturate it at 5 K than at room temperature, and had a saturation magnetization of 1.7 μ_B/Fe, which is almost twice that of the STF40 sample. The coercivity of La30 was 1000 Oe, also larger than the coercivity of the STF40 sample. The magnetoelastic effects are assumed to persist since

dx.doi.org/10.1021/ic301726w | Inorg. Chem. 2012, 51, 13245−13253

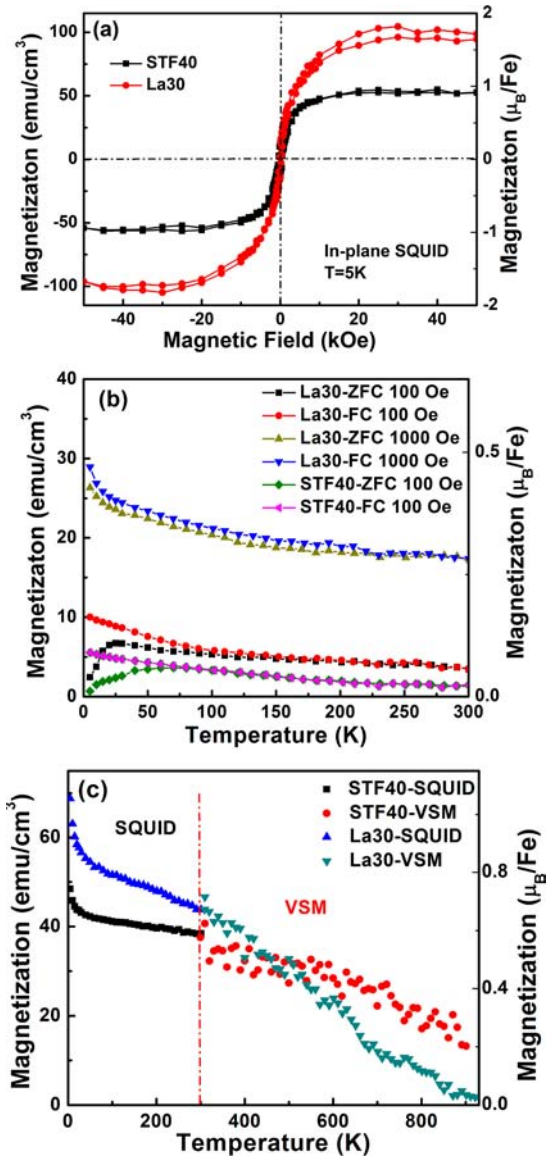

Figure 8. Low temperature hysteresis loops of LaSTF films characterized by SQUID: (a) in-plane hysteresis loops for $x = 0$, and $x = 0.3$ at 5 K from −50 kOe to +50 kOe; (b) the field-cooled and zero-field-cooled magnetization versus temperature curves for $x = 0$ at 100 Oe, $x = 0.3$ at 100 Oe and $x = 0.3$ at 1000 Oe; (c) the in-plane magnetization-temperature curve of films with $x = 0$ and $x = 0.3$ from 5 to 1000 K measured at 8 kOe.

the films maintain an out-of-plane anisotropy at low temperature.

Low temperature zero-field-cooled and field-cooled (ZFC-FC) magnetization curves of La30 and STF40 films measured at 100 and 1000 Oe are shown in Figure 8b. At 100 Oe applied field, a divergence of the FC and ZFC curves was observed for the La30 and for the STF40, while at 1000 Oe, the La30 ZFC curve did not show a maximum. Low field FC/ZFC divergence was seen previously for single crystal STF films at 100 Oe[7,21] and attributed to spin-glass behavior from competing interactions between mixed-valence Fe. Figure 8c shows temperature dependence of the magnetization for STF40 and La30 films with an applied field of 8 kOe perpendicular to the plane. These curves did not follow the Brillouin function expected from magnetic materials dominated by exchange, and the more gradual decrease in magnetization with temperature has been interpreted for similar STF films using a magnetoelastic model.[9] The magnetization vanished at T_C = ~900 K for La30, and even higher for STF40, which can be compared to STF40/$LaAlO_3$, which had a T_C near 1000 K.[7]

IV. CONCLUSIONS

Perovskite-structured $(Ce_xSr_{1-x})(Ti_{0.6}Fe_{0.4})O_{3-\delta}$ ($x = 0$, 0.1, 0.2 and 0.3) and $(La_xSr_{1-x})(Ti_{0.6}Fe_{0.4})O_{3-\delta}$ (x = 0,0.1,0.2,0.3 and 0.4) films grown epitaxially on LSAT substrates show room temperature ferromagnetism of 0.6−0.8 μ_B/Fe, an out-of-plane anisotropy attributed to magnetoelasticity and a Faraday rotation of 900−1800 deg/cm at 1.55 μm wavelength. The films were under in-plane compression, and the Ce-substituted films showed a layer of partial strain relaxation. There was no evidence for compositional inhomogeneity or clustering. Ce (mainly Ce^{3+}) and La substituted for Sr^{2+} and acted as donors, and at 30% Ce the film exhibited n-type conductivity. With increasing Ce and La concentration, the optical band gap widened, the Fermi level shifted toward the vacuum level and Fe was driven to a lower valence state. La and Ce substitutions above about 30% increased the saturation magnetization by ~20% and the Faraday rotation by up to 100%, but also increased the optical absorption in the near-IR, lowering the magneto-optical figure of merit. These results are discussed in terms of an increase in the population of low-valence Fe ions with Ce and La A-site substitution.

AUTHOR INFORMATION

Corresponding Author

*E-mail: peng0469@gmail.com (P.J.), caross@mit.edu (C.A.R.).

Notes

The authors declare no competing financial interest.

ACKNOWLEDGMENTS

The authors are grateful to Mr. K. V. Raman for his help in electronic transport characterization. This work was supported by the National Science Foundation, Division of Materials Research. A Fellowship from the Chinese Scholarship Council is gratefully acknowledged. This work made use of the MRSEC Shared Experimental Facilities supported by the National Science Foundation under Award No. DMR-0819762.

REFERENCES

(1) Geller, S.; Gilleo, M. A. *J. Phys. Chem. Solids* **1957**, *3*, 30.
(2) Boudiar, T.; Payet-Gervy, B.; Blanc-Mignon, M.-F.; Rousseau, J.-J.; Le Berre, M.; Joisten, H. *J. Magn. Magn. Mater.* **2004**, *284*, 77−85.
(3) Xu, B.; Yin, K. B.; Lin, J.; Xia, Y. D.; Wan, X. G.; Yin, J.; Bai, X. J.; Du, J.; Liu, Z. G. *Phys. Rev. B* **2009**, *79*, 134109.
(4) Rajamani, A.; Dionne, G. F.; Bono, D.; Ross, C. A. *J. Appl. Phys.* **2005**, *98*, 063907.
(5) Maier, R.; Cohn, J. L. *J. Appl. Phys.* **2002**, *92*, 5429.
(6) Matsui, T.; Sato, R.; Tsuda, H. *J. Appl. Phys.* **2008**, *103*, 07E304.
(7) Kim, H. S.; Bi, L.; Dionne, G. F.; Ross, C. A. *Appl. Phys. Lett.* **2008**, *93*, 092506.
(8) Leung, G. W.; Vickers, M. E.; Fix, T.; Blamire, M. G. *J. Phys.: Condens. Matter* **2009**, *21*, 426003.
(9) Bi, L.; Kim, H. S.; Dionne, G. F.; Ross, C. A. *New J. Phys.* **2010**, *12*, 043044.
(10) Balamurugana, K.; Harish Kumara, N.; Arout Chelvaneb, J.; Santhosh, P. N. *J. Alloys Compd.* **2009**, *472*, 9.
(11) Jiang, P.; Bi, L.; Kim, D. H.; Dionne, G. F.; Ross, C. A. *Appl. Phys. Lett.* **2011**, *98*, 231909.

(12) Kim, D. H.; Bi, L.; Jiang, P.; Dionne, G. F.; Ross, C. A. *Phys. Rev. B* **2011**, *84*, 014416.
(13) Kim, D. H.; Bi, L.; Aimon, N. M.; Jiang, P.; Dionne, G. F.; Ross, C. A. *ACS Comb. Sci.* **2012**, *14*, 179.
(14) Kim, H.-S.; Bi, L.; Paik, H.; Yang, D.-J.; Park, Y. C.; Dionne, G. F.; Ross, C. A. *Nano Lett.* **2010**, *10*, 597−602.
(15) Onoda, M.; Yasumoto, M. *J. Phys.: Condens. Matter* **1997**, *9*, 5623.
(16) Yamada, Y. F.; Ohtomo, A.; Kawasaki, M. *Appl. Surf. Sci.* **2007**, *254*, 768.
(17) Shannon, R. D.; Prewitt, C. T. *Acta Crystallogr.* **1969**, *B25*, 925.
(18) Chambers, S. A.; Liang, Y.; Yu, Z.; Droopad, R.; Ramdani, J. *J. Vac. Sci. Technol., A* **2001**, *19*, 934.
(19) Marshall, M. S. J.; Newell, D. T.; Payne, D. J.; Egdell, R. G.; Castell, M. R. *Phys. Rev. B* **2011**, *83*, 035410.
(20) Xiao, W.; Guo, Q.; Wang, E. G. *Chem. Phys. Lett.* **2003**, *368*, 527.
(21) Kim, H.-S.; Bi, L.; Kim, D. H.; Yang, D.-J.; Choi, Y. J.; Lee, J. W.; Kang, J. K.; Park, Y. C.; Dionne, G. F.; Ross, C. A. *J. Mater. Chem.* **2011**, *21*, 10364.
(22) Eerenstein, W.; Morrison, F. D.; Dho, J.; Blamire, M. G.; Scott, J. F.; Mathur, N. D. *Science* **2005**, *307*, 1203a.
(23) Fujii, T.; de Groot, F. M. F.; Sawatzky, G. A. *Phys. Rev. B* **1999**, *59*, 3195−3202.
(24) Grosvenor, A. P.; Kobe, B. A.; Biesinger, M. C.; McIntyre, N. S. *Surf. Interface Anal.* **2004**, *36*, 1564−1574.
(25) Hüfner, S. In *Photoelectron Spectroscopy*, 3rd ed.; Springer-Verlag: Berlin, 2003; Chapter 2, p 65.
(26) Ino, A.; Mizokawa, T.; Fujimori, A. *Phys. Rev. Lett.* **1997**, *79*, 2101.
(27) Dionne, G. F.; Bi, L.; Kim, H.-S.; Ross, C. A. *J. Appl. Phys.* **2011**, *109*, 07B761.
(28) Tsui, E.; Smoak, M. C.; Nath, T. K.; Eom, C. B. *Appl. Phys. Lett.* **2000**, *76*, 2421.
(29) Wang, Z.-H.; Kronmüller, H.; Lebedev, O. I.; Gross, G. M.; Razavi, F. S.; Habermeier, H.-U.; Shen, B. G. *Phys. Rev. B* **2002**, *65*, 054411.
(30) Rao, R. A.; Lavric, D.; Nath, T. K.; Eom, C. B.; Wu, L.; Tsui, F. *Appl. Phys. Lett.* **1998**, *73*, 3294.
(31) Valencia, S.; Balcells, L. I.; Martínez, B.; Fontcuberta, J. *J. Appl. Phys.* **2003**, *93*, 8059.
(32) Dionne, G. F. *J. Appl. Phys.* **1979**, *50*, 4263.
(33) Falkovskaya, L. D.; Fishman, A.Ya.; Ivanov, M. A.; Mitrofanov, V. Ya. *J. Magn. Magn. Mater.* **1988**, *71*, 337.
(34) Takamura, Y.; Yang, F.; Kemik, N.; Arenholz, E.; Biegalski, M. D.; Christen, H. M. *Phys. Rev. B* **2009**, *80*, 180417.
(35) Takamura, Y.; Chopdekar, R. V.; Scholl, A.; Doran, A.; Liddle, J. A.; Harteneck, B.; Suzuki, Y. *Nano Lett.* **2006**, *6*, 1287.
(36) Dionne, G. F.; Kim, H.-S. *J. Appl. Phys.* **2008**, *103*, 07B333.
(37) Kim, D. H.; Aimon, N. M.; Bi, L.; Florez, J. M.; Dionne, G. F.; Ross, C. A. *J. Phys.: Condens. Matter* **2013**, *25*, 026002.
(38) Shintaku, T.; Tate, A.; Mino, S. *Appl. Phys. Lett.* **1997**, *71*, 1641.
(39) Zhao, W. *Sens. Actuators, A* **2001**, *89*, 252.
(40) Lucari, F.; Terrenzio, E.; Tomassetti, G. *J. Appl. Phys.* **1981**, *52*, 2301.
(41) Lucari, F.; Mastrogiuseppe, C.; Tomassetti, G. *J. Phys. C: Solid State Phys.* **1977**, *23*, 4869.
(42) Blasse, G.; Dirksen, G. J. *J. Solid State Chem.* **1981**, *37*, 390.
(43) Swanepoel, R. *J. Phys. E: Sci. Instrum.* **1983**, *16*, 1216.
(44) Hu, B.-Q.; Wang, X.-M.; Zhou, T.; Zhao, Z.-Y.; Wu, X.; Chen, X.-L. *Chin. Phys. Lett.* **2001**, *18*, 278.
(45) Bisceglia, B.; De Leo, R.; pia Pastore, A.; von Gratowski, S.; Meriaki, V. *J. Microwave Power Electromagn. Energy* **2011**, *45*, 37.